Sensors and Materials, Vol. 36, No. 7 (2024) 2965–2982
MYU Tokyo

S & M 3713

Remote-sensing-based Approach to Analysis of Thermal Environment for Island-type City

Yankun Chen,[1] Chao Chen,[2*] Jiayin Yang,[3] Zhisong Liu,[1] and Taohua Ren[1]

[1]School of Information Engineering, Zhejiang Ocean University, Zhoushan 316022, China
[2]School of Geography Science and Geomatics Engineering, Suzhou University of Science and Technology, Suzhou 215009, China
[3]Geography Department, University College London, London WC1E 6BT, United Kingdom

(Received February 16, 2024; accepted June 3, 2024)

Keywords: impact analysis, land surface temperature retrieval, satellite remote sensing, spatiotemporal characteristics, urban heat island

How to rapidly and effectively monitor the distribution and intensity of the urban thermal field in island-type cities, especially for understanding the impact of human activities on the urban thermal environment, is an urgent need to address environmental issues. Satellite remote sensing and geographical information system (GIS) techniques are used to retrieve the land surface temperature (LST), analyze the urban heat-island (UHI) effect to clarify its spatiotemporal characteristics and evolution rules, and clarify the impact of human activities on the thermal environment of an island-type city. The validity and applicability of the proposed method are demonstrated experimentally on Zhoushan Island, China. (1) The surface temperature of Zhoushan Island gradually decreases from the surrounding to the interior, high-temperature areas are mainly distributed in highly urbanized coastal areas with frequent human activities, and low-temperature areas are mainly distributed in interior regions with high vegetation coverage. (2) During the study period, the proportion of heat-island areas increases gradually, and areas with high heat-island levels are mainly distributed in the highly urbanized areas along the coast. (3) The proportion of heat-island of different levels changes negligibly, while moderate-temperature areas evolve into higher level heat-island areas. (4) LST and the UHI effect are negatively correlated with vegetation coverage and positively correlated with the density of urban buildings. The results of this study provide data support for urban planning and are of great significance for the sustainable development of sea island cities.

1. Introduction

In recent years, the continuous rise in global temperature has resulted in climate anomalies and the degradation of ecological environments, posing threats to human survival.[1–4] In addition, the increasing urban population and the scale of urban construction also aggravate the intensity of urban heat islands (UHIs), affecting public health and air quality and resulting in the

*Corresponding author: e-mail: chenchao@usts.edu.cn
https://doi.org/10.18494/SAM5024

ISSN 0914-4935
https://myukk.org/

increased consumption of all types of energy, which has a direct impact on human life.[5–8] On islands, the level of the heat-island effect can directly reflect the cumulative effect of human activities on the UHI effect.[9–11] Few researchers have studied the UHI effect of islands because the natural advantage of islands surrounded by the sea causes people to ignore the possibility of the UHI effect.[12,13] Therefore, timely and accurate knowledge of UHIs in island areas will help alleviate the serious economic, ecological, and public health problems caused by the UHI effect and promote the sustainable development of island areas.

The study of UHIs has more than one hundred years of history, and the research methodology, which is a phased approach, has been gradually completed.[14,15] First, to maintain the continuity of the time scale, scientists chose to use surface meteorological data to study UHIs, which mainly includes two research areas: urban canopy heat islands and urban boundary layer heat islands.[16–18] Although this method has good continuity, the discrete point data and linear data stacking cannot be directly equated to the surface temperature plane data. In addition, there are still some problems such as the unclear analysis of internal structure characteristics, the neglect of the urban layout, and the low precision of scale conversion. Since then, the other methods used to study UHIs have been put forward, such as the fixed point observation, meteorological, moving transect, remote-sensing monitoring, and model simulation methods. The fixed point observation method allows the direct measurement of temperature differences at specific locations but is labor-intensive.[19,20] The meteorological method uses the weather station network to monitor the temperature of the city and surrounding areas, providing reliable long-term data, but it cannot provide high-resolution data, and the site layout cannot cover the entire city.[21] In the combined use of mobile sensors and meteorological data, the moving transect method can provide a more comprehensive UHI image, but it requires a high economic cost.[22,23] After a long period of verification, the meteorological and remote-sensing monitoring methods are found to have the ability to monitor UHIs over a large range as well as good applicability and accuracy. Thus, they are widely used by experts and scholars.[24–27]

Land surface temperature (LST) plays an important role in the process of energy exchange between the land surface and the atmosphere, and has important research value in the fields of surface radiation energy balance, global climate change, urban thermal environment, and resource environment monitoring.[28–30] Recently, Jallu *et al.* even have explored the impact of COVID-19 on different land cover types in surface heat-islands and found that the average surface temperatures in New Delhi, Hyderabad, and Mumbai in April 2020 (post-lockdown) decreased by 5, 1.9, and 0.26 °C, respectively, compared with the pre-lockdown period in 2019.[31] Their study revealed that the virus-induced chain reaction, which was characterized by diminished human activities leading to the temporary closure of numerous factories, public facilities, and buildings, significantly mitigated the UHI effect, underscoring its substantial humanistic and social implications. LST is a key factor in studying the process of the UHI effect.[32] Since the surface temperature cannot be detected artificially or by instruments, remote-sensing retrieval is generally performed in scientific research.[33–35] With the wide application of satellite image data in various fields, the progress of thermal infrared remote-sensing technology and the rapid development of remote-sensing technology make it practical to monitor LST over a large range conveniently.[36–39] Since the 1960s, both domestic and

internation scholars have explored LST retrieval methods for remote-sensing data, atmospheric correction-based methods, and single-channel, monowindow, split-window, and multichannel algorithms, to name a few.[40] On the basis of these algorithms, many improved algorithms have been developed in accordance with the characteristics of specific data and the actual situation in the application.[41,42] Among these, the monowindow algorithm stands out as the simplest and most straightforward method; it was derived on the basis of the surface heat radiative conduction equation taking into consideration the specific characteristics of Landsat TM 6.[43] This algorithm only requires three parameters, atmospheric transmittance, surface emissivity, and average atmospheric temperature, to retrieve surface temperature. This method has been widely used with high accuracy. It has become the most representative LST remote-sensing retrieval algorithm among monowindow algorithms and is widely used by scholars and research experts. Satellites and sensors using remote-sensing data for LST retrieval are gradually increasing in number, such as Landsat-8, Tiangong-2, GF-5, and FY series satellites. The research is concentrated in developed cities such as Beijing, Shanghai, Hangzhou, Jinan, Shijiazhuang, Nanjing, and other populous urban centers. In addition, some experts have selected representative sites, such as Fuzhou (surrounded by mountains), Pingxiang (pilot city for sponge city construction), and Dongchangfu in Liaocheng (known for having the largest artificial urban freshwater lake).

In this work, the remote-sensing monitoring method is used to study the heat-island effect of island-type cities, LST data are obtained via Landsat thermal infrared data retrieval, and the mean and standard deviation of temperature are used to determine the threshold to delineate the heat-island area, calculate the heat-island intensity, and analyze its relationship with natural factors (NDVI) and human activities (NDBI). Zhoushan Island is selected to carry out the verification experiment. The results of this study can provide data support and technical support for urban scientific management and regional planning.

2. Study Area and Datasets

2.1 Study area

Zhoushan City is the only provincial-level prefecture composed of an archipelago consisting of 2085 islands with a total area of 22200 km^2. Among them, Zhoushan Island is the fourth largest island in China after Taiwan Island, Hainan Island, and Chongming Island.[44] It is shaped like a boat, lying slightly from the northwest to the southeast, with a maximum length of 44 km and a maximum width of 18 km.[45,46] It is located at the intersection of the golden coastline of eastern China and the golden waterway of the Yangtze River, backed by the vast economic basin of the Yangtze River Delta. The climate is typical of the subtropical ocean monsoon zone and is highly seasonal, being hot and rainy in summer and mild in winter. The location of Zhoushan Island is shown in Fig. 1.

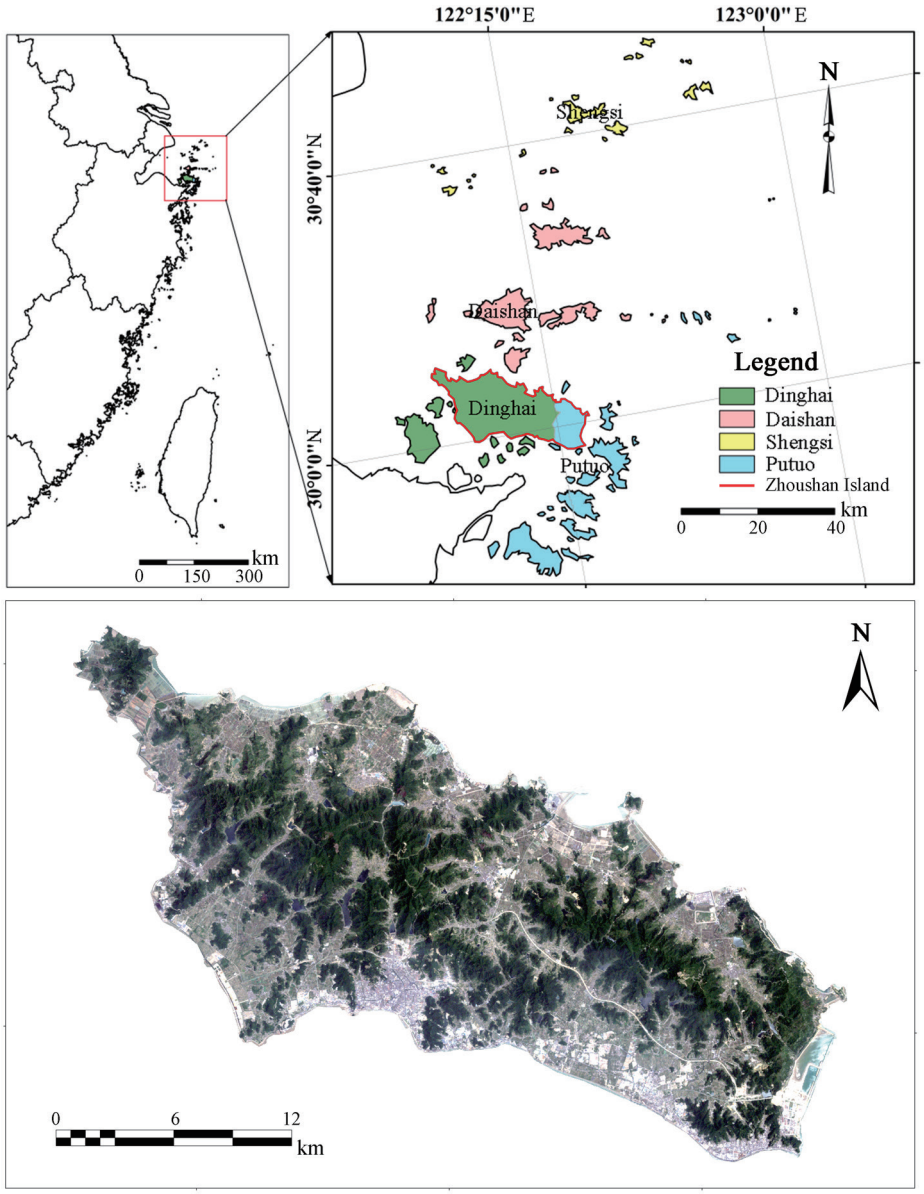

Fig. 1. (Color online) Location of study area. The base map is a true color composite of Landsat 8 images that rank band composites in the order of red, green and blue bands.

2.2 Datasets

The Landsat program is a land-based satellite project jointly implemented by the National Aeronautics and Space Administration (NASA) and the United States Geological Survey (USGS).[47,48] Since the successful launch of Landsat 1 on 23 July 1972, the United States has developed and launched eight more satellites in the Landsat series (Landsat 6 failed).

In this study, five years of Landsat satellite data from 2000 to 2020 are selected for research, and the specific information is shown in Table 1. The data are from Geospatial Data Cloud (http://www.gscloud.cn/search) and Glovis (https://glovis.usgs.gov).

3. Methodology

In this study, the thermal infrared band of Landsat images is used to retrieve LST, delineate the intensity of the UHI, distinguish the spatial extent of the UHI, and clarify the characteristics of the spatial and temporal distributions of the UHI on Zhoushan Island. Using optical bands, the normalized difference vegetation index (NDVI) and normalized difference built-up index (NDBI) are calculated to analyze the impact of human activities on the urban thermal environment. This study mainly consists of the following steps. (1) Remote-sensing images covering the study area from 2000 to 2020 are selected and subjected to radiometric calibration, atmospheric correction, and other operations. (2) The land surface temperature is retrieved, the threshold to divide the heat-island area is determined, and the urban heat intensity is calculated. (3) The heat-island proportion map is combined with the urban heat intensity distribution to analyze the spatial and temporal distribution characteristics of the heat-island in Zhoushan, and then, the NDVI and NDBI are calculated to carry out correlation analysis. The detailed technical process is shown in Fig. 2.

3.1 Preprocessing of data

There are many bands of remote-sensing data in the Landsat series, and the problems of "same-spectrum foreign matter and same object but different spectrum in surface cover" easily occur in the process of extracting ground objects. Therefore, the direct use of original images can cause distortion and errors in actual research. This is why preprocessing is particularly important. First, images covering the study area from 2000 to 2020 with good imaging quality are selected. Subsequently, radiometric calibration and atmospheric correction are performed. Radiation calibration is an important part of remote-sensing image preprocessing, and its function is to obtain the absolute radiation luminance value and other physical quantities. The effect of atmospheric correction is to eliminate the radiation errors caused by atmospheric aerosols, cloud particle absorption, atmospheric scattering, and illumination in remote-sensing

Table 1
Information of thermal infrared data from the Landsat satellite.

Imaging time	Satellite	Sensor	Band	Spatial resolution (m)
2000.09.18	Landsat 5	Thematic Mapper	Band 6 Thermal (10.40–12.50 μm)	120
2005.06.04 2011.05.20	Landsat 7	Enhanced Thematic Mapper Plus	Band 6 Thermal (10.40–12.50 μm)	60
2015.08.03 2020.08.16	Landsat 8	Thermal Infrared Sensor	Band 10 TIRS1 (10.6–11.19 μm) Band 11 TIRS2 (11.5–12.51 μm)	100

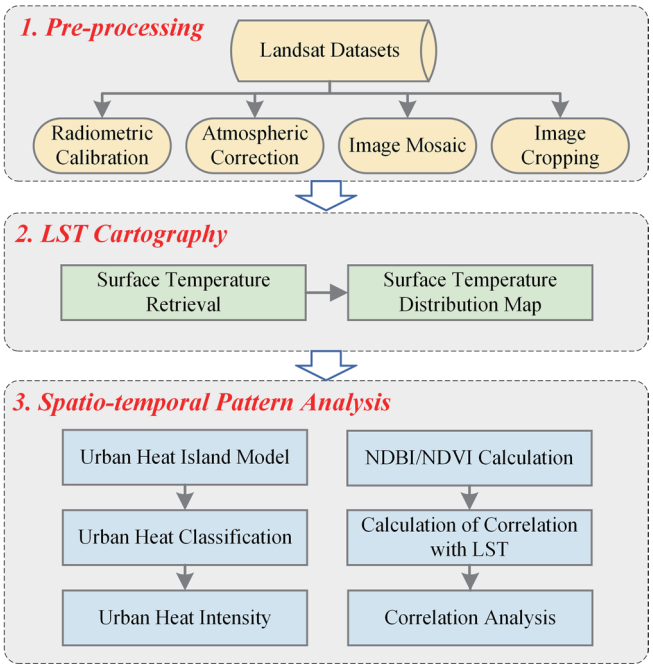

Fig. 2. (Color online) Flowchart of technical process.

image preprocessing in order to realize the retrieval of the real surface reflectance of the ground object. The FLAASH model is used for the atmospheric correction of the process in this research.

3.2 LST retrieval and UHI determination

3.2.1 LST retrieval

In this research, the atmospheric correction method is used to retrieve LST. The atmospheric correction method, also known as the radiative transfer equation (RTE) method, is based on the principle that the thermal radiation received by the satellite sensor is mainly composed of three parts: the upward radiation of the ground, the radiation of the atmosphere reflected by the ground to the sensor, and the upward radiation of the atmosphere.[49,50] To obtain accurate ground thermal radiation values, it is necessary to remove the effect of atmospheric action received by the satellite sensor. Such elimination mainly includes two methods: one is to estimate the effect of the atmosphere on the thermal radiation of the surface using algorithms such as MODTRAN, LOWTRAN, and 6S, and the other is to directly obtain the measured atmospheric profile data consistent with the satellite transit time. Finally, the surface thermal radiation removed by atmospheric action is retrieved from the real surface temperature. The calculation formula of the RTE method is

$$L_{sensor} = [\varepsilon B(T_S) + (1 - \varepsilon L_{atm\downarrow})]\tau + L_{atm\uparrow}, \tag{1}$$

where L_{sensor} is the radiation received by the satellite sensor (w / (m^2 · sr · μm)); ε is the land surface emissivity; $B(T_S)$ is the blackbody radiation; T_S is the land surface temperature (K); $L_{atm\downarrow}$ is the atmospheric downward irradiance; $L_{atm\uparrow}$ is the atmospheric upward irradiance; and τ is the atmospheric transmissivity.

The surface temperature can be calculated using Planck's formula, which is given by

$$T_S = \frac{K_2}{\ln\left[\frac{K_1}{B(T_S)} + 1\right]}, \tag{2}$$

where T_S is the land surface temperature (K) and K_1 and K_1 are constants. For different Landsat data, K_1 and K_1 take different values:

For Landsat 5 TM, K_1 = 606.76 W/(m^2 × sr × μm), K_2 = 1260.56 K.
For Landsat 7 ETM+, K_1 = 666.09 W/(m^2 × sr × μm), K_2 = 1282.71 K.
For Landsat 8 OLI/TIRS, K_1 = 774.89 W/(m^2 × sr × μm), K_2 = 1321.14 K.

3.2.2 Grade distribution of UHI and urban heat intensity calculation

Understanding the distribution of UHIs not only offers pertinent climate information for urban planning and design, ensuring that buildings and infrastructure are more resilient to climate change, but also contributes to enhancing the quality of life, health, and social well-being of urban residents. In this study, surface temperature is categorized into seven categories using the mean-standard deviation method, and the two highest and two lowest heat-island categories are combined separately. The specific formula is

$$T = A \pm X \cdot sd, \tag{3}$$

where T represents the calculated temperature threshold; A is the mean surface temperature of the study area; sd is the standard deviation of the surface temperature of the study area; and X is a multiple of the standard deviation and takes the value of 0.5, 1.0, or 1.5.

On the basis of the above formula, the UHI grade in the study area can be categorized into six categories: strong heat-island, stronger heat-island, moderate-temperature, weaker heat-island, weak heat-island, and no heat-island areas.

Furthermore, urban heat intensity data are calculated. Such data can be used to provide guidance for urban planning and to help planners better understand the degree and distribution of the UHI effect in order to take corresponding measures to improve the environment. In addition, they can be used to monitor, assess, and quantify the severity of the UHI effect and can

provide critical information about intracity temperature differences for climate adaptation, environmental protection, and health research. Heat-island intensity refers to the difference between the average surface temperatures of high-density urbanized areas and suburban areas (areas with high vegetation coverage).[51,52] The specific formula is

$$UH\_INT = LST_u - LST_s, \tag{4}$$

where UH_INT is the urban heat intensity; LST_u is the average LST of high-density urban built-up areas; and LST_s is the average LST of suburban areas. According to the actual situation of surface temperature inversion in Zhoushan City, LST_u is taken as the average regional surface temperature for $NDBI > 0.02$ and LST_s is taken as the average regional surface temperature for $NDVI > 0.5$.

3.3 Analysis of anthropogenic impacts on the urban thermal environment

The UHI effect is significantly related to air temperature, and *NDVI* and *NDBI* can consequently reflect urban heat intensity and land cover type. Therefore, analyzing the correlation between them can reveal the climate impact of UHIs and help researchers better understand urban climate change, contributing to the achievement of urban sustainability goals.

3.3.1 Calculations of NDVI and NDBI

NDVI as a common remote-sensing index is used to evaluate the condition and distribution of vegetation on the land surface.[53,54] It is widely used in environmental monitoring, agriculture, forestry, urban planning, meteorology, geology, and other fields. *NDVI* is mainly calculated by analyzing the reflection of visible and near-infrared wavelengths. The calculation formula is

$$NDVI = \frac{NIR - RED}{NIR + RED}, \tag{5}$$

where *NIR* is the reflection of the near-infrared band and *RED* is the reflection of the red band.

NDBI is a kind of index used in remote sensing and telemetry to identify and evaluate building cover on the ground. It is often used in urban planning, land use research, urban expansion monitoring, building change detection, and disaster assessment. The calculation formula is

$$NDBI = \frac{MIR - NIR}{MIR + NIR}, \tag{6}$$

where *NIR* is the reflection of the near-infrared band and *MIR* is the reflection of the mid-infrared band.

3.3.2 Impact analysis

Since LST is strongly correlated with vegetation and the degree urban construction (LST is low in areas with high vegetation coverage and high in areas with high urban built-up areas), the retrieved LST can be correlated with *NDVI* and *NDBI* to calculate the correlation coefficient. We use the Pearson correlation coefficient to measure the correlations between *LST* and *NDVI* as well as between *LST* and *NDBI*. The Pearson correlation coefficient takes a value between -1 and 1, with values close to 1 indicating a positive correlation, values close to -1 indicating a negative correlation, and values close to 0 indicating no correlation.

4. Results and Analysis

4.1 LST retrieval

LST retrieval is a process of estimating the earth surface temperature using remote-sensing technology or model. This process can provide valuable data support for monitoring the changing trend of earth surface temperature and necessary information for the study of the UHI effect. In this study, remote-sensing images of five periods (September 2000, June 2005, May 2011, August 2015, and August 2020) are selected for LST retrieval, and the results are shown in Fig. 3.

Figure 3 shows that the surface temperature of Zhoushan Island exhibits the trend of being high around the periphery and low in the interior. High-temperature areas are predominantly found along the coastal areas of Zhoushan Island and identified as built-up areas when cross-referenced with the satellite image in Fig. 1. This reveals a greater correlation between higher surface temperature and human activities.

To better understand the climate change of Zhoushan Island and deeply analyze the change of the heat-island effect in Zhoushan Island, the interannual mean and standard deviation of surface temperature in Zhoushan Island are statistically calculated and shown in Table 2.

Figure 4(a) and Table 2 show that the average surface temperature in 2000 was 31.12 ℃, the water body temperature was basically maintained at 20.00–30.00 ℃, and the temperature in the central area of high dense vegetation was about 30.00 ℃, which was slightly lower than that in the surrounding agricultural areas. In general, there is no significant difference in temperature between areas. The results show that the temperature gap between the high-vegetation-cover areas and the rural areas was small in 2000, and the human activities in the suburban areas had no significant effect on the increase in surface temperature. The distribution of the high-temperature areas in the middle is scattered, and there is a clear delineation between the high-temperature areas and the outer area, which is due to the scattered distribution of villages under the characteristics of vegetation cover. The outer high-temperature areas are mainly distributed in the south and southeast of Zhoushan Island, which are the high-density urban built-up areas in Dinghai District and Putuo District, and their surface temperatures are above 40.00 ℃.

Figure 4(b) and Table 2 show that the average surface temperature of Zhoushan Island in 2005 was 30.23 ℃, which was slightly lower than that in 2000. This difference may be attributed

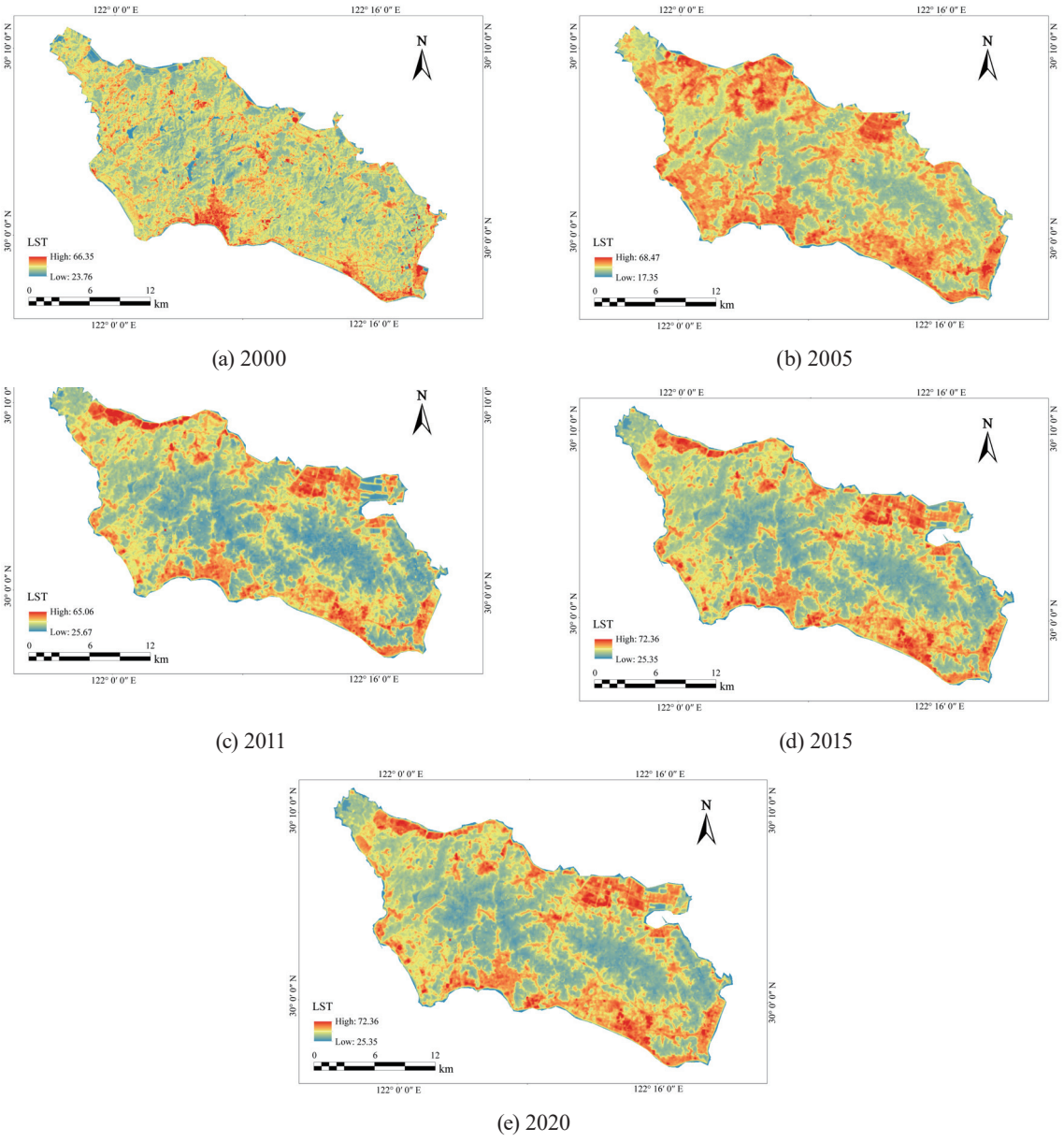

Fig. 3. (Color online) Retrieval results of LST from 2000 to 2020.

Table 2
Mean and standard deviation of land surface temperature from 2000 to 2020 (°C).

	2000	2005	2011	2015	2020
Mean	31.12	30.23	32.12	37.29	40.43
Standard deviation	1.61	2.11	2.92	3.02	3.45

to seasonal factors. In the subtropical monsoon climate, the overall temperature in June is usually lower than that in September. However, in 2005, the number of high-temperature areas increased markedly, and the distribution tended to be more concentrated, from scattered high-temperature areas to more dense block areas. In addition, the high-temperature areas were more widespread in 2005, covering almost all regions, including the southwest, west, and north, which

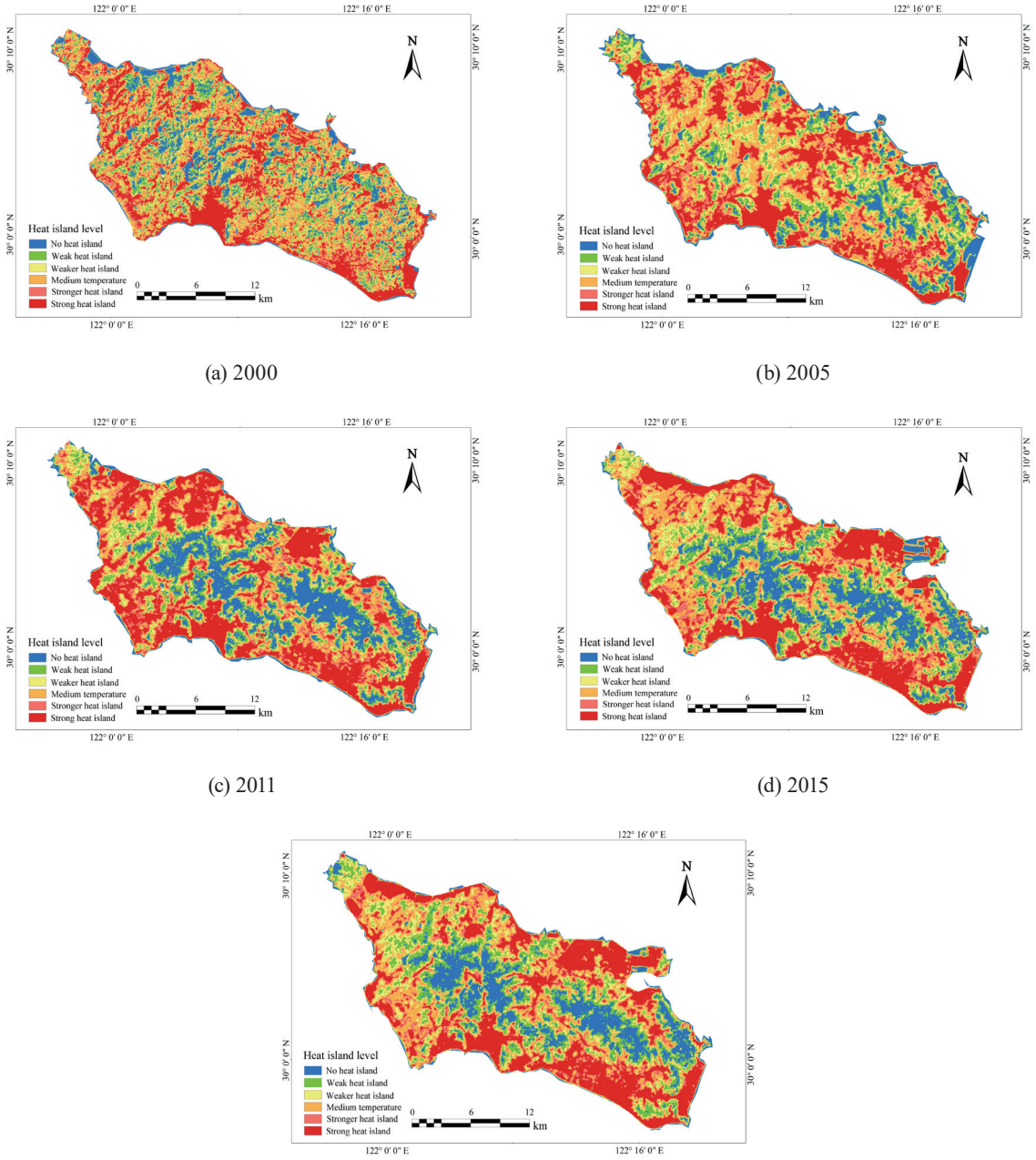

(a) 2000 (b) 2005

(c) 2011 (d) 2015

(e) 2020

Fig. 4. (Color online) Heat-island classification maps from 2000 to 2020.

did not have significantly high temperatures in 2000. Compared with 2000, the range of high-temperature areas in the central region of the island expanded and obviously extended outward.

Figure 4(c) and Table 2 show that the average surface temperature of Zhoushan Island in 2011 was 32.12 °C, which was 2.00 °C higher than that in 2005. Compared with Figs. 4(a) and 4(b), vegetation-covered and urbanized areas showed a more significant temperature difference in 2011. The average temperature in the central vegetated areas was about 30 °C, and the extent of the urban high-temperature areas expanded compared with 2005, transitioning from block areas

to planar areas. In addition, the temperature of the high-temperature areas in the north and northwest increased significantly, up to 50.00 ℃, while the temperature in the western high-temperature areas was relatively stable and the range expanded slightly. The urban built-up areas in the southeast and south still showed high temperature characteristics in 2011, but there was no significant change compared with 2000 and 2005.

Figure 4(d) and Table 2 show that the average surface temperature of Zhoushan Island rose sharply in 2015, reaching 37.29 ℃. However, this change was also affected by climate factors, because the average temperature in August is usually the highest in the annual temperature data. In terms of temperature distribution, the temperature difference between the inland vegetated areas and the urban built-up areas increases significantly, and the overall temperature shows a decreasing trend from the outside to the interior. The high-temperature areas in the southwest significantly decreased in scope compared with that in 2011, while the high-temperature areas in the northwest also decreased in scope, but their distribution was more dense and their temperature was higher. As can be seen from Fig. 4(d), the high-temperature areas were basically consistent with the coastline, indicating that the urban construction in the northwest gradually had moved toward the coastline since 2011. In the northeast, because of the expansion of Zhoushan Island, the high-temperature areas also expanded.

From both Fig. 4(e) and Table 2, it can be seen that the average surface temperature of Zhoushan Island in 2020 was still elevated, reaching 40.43 °C. The temperature distribution was roughly the same as that in 2015, with a slight expansion of the range of high-temperature areas, especially in the northeastern built-up expansion areas, and the range of high-temperature areas in the southeastern urban built-up areas of Putuo was also more extensive than in 2015. Overall, the temperature difference between the vegetation-covered areas and the urban built-up areas on the island was more significant in 2020. This may be due to seasonal factors: vegetation growth is at its peak in August, and the heat dissipation effect of plants and soil on the surface is more pronounced.

4.2 Analysis of the UHI effect

4.2.1 Grade distribution of UHI

The UHI effect might have negative effects on the health of residents and the environment. By categorizing the heat-island, it is possible to accurately locate the areas affected by severe UHI effects, so that appropriate measures can be taken to improve air quality, reduce heat stress, and improve the living environment. With an in-depth understanding of the distribution of heat islands in different areas within cities, urban planners and governments can manage urban resources more effectively and formulate more targeted urban planning policies to reduce the negative impact of the UHI effect.

In this study, the UHIs of Zhoushan Island are categorized into six categories using the mean-standard deviation method, the grade distribution maps of the UHIs, and the percentage of each area (in September 2000, June 2005, May 2011, August 2015, and August 2020) and are plotted and statistically calculated, as shown in Figs. 4 and 5.

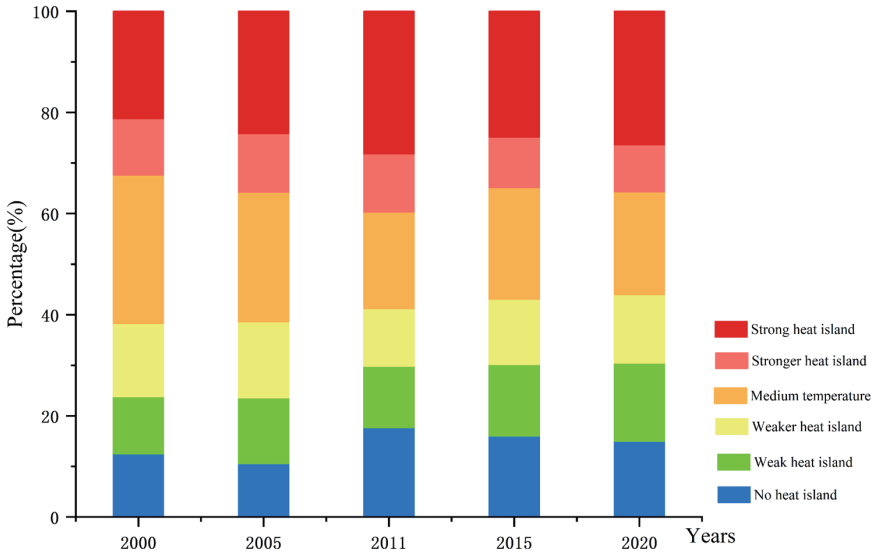

Fig. 5. (Color online) UHI grade distributions from 2000 to 2020.

Figure 4 shows the characteristics of heat-island distribution. The strong heat-island areas are mainly concentrated in urban built-up and suburban built-up areas. The no heat-island and weak heat-island areas are mainly concentrated in the areas of highly dense vegetation, water bodies, and agricultural development areas, while the moderate-temperature areas are the transition areas between weak and strong heat islands. In 2000, the distributions of strong and stronger heat islands were scattered, but gradually became concentrated over time. The stronger heat-island areas are gradually spreading to coastal areas. The distributions of heat-island levels in 2011, 2015, and 2020 were relatively consistent, and the distribution areas of heat islands of the same level also showed a high degree of consistency, indicating that the pattern of UHIs on Zhoushan Island has been gradually becoming finalized since 2011.

The proportions of different categories of UHI on Zhoushan Island in Fig. 5 show that the proportion of areas of strong heat-island intensity increased gradually with time. There is no obvious difference between the proportions of weak heat, weaker heat, and strong heat islands in the 20-year time-series observation. However, the proportion of moderate-temperature areas gradually decreased, indicating that the moderate-temperature areas gradually changed into stronger and strong heat-island areas. Compared with 2000, there was no significant change in the proportion of heat-island intensity areas in 2005, but the proportion of no heat-island areas decreased and that of weak heat-island areas increased, indicating that some of the no heat-island areas were transforming into weak heat-island areas. However, the proportions of no and strong heat-island areas reached their maximum in 2011, showing that the UHI effect was the most severe in 2011. The proportions of UHIs in 2015 and 2020 were basically the same, but the proportion of strong heat islands in 2020 increased by 1.47% compared with 2015. Furthermore, the proportions of areas unaffected by the UHI effect in 2011, 2015, and 2020 were marginally higher than in the preceding years. These areas are predominantly found in regions with dense vegetation, highlighting the significant impact of extensive vegetation coverage on mitigating the UHI phenomenon.

4.2.2 Intensity analysis of UHI

To measure the difference in *LST* between urban areas and the surrounding countryside and quantify the extent of the UHI effect, the urban heat intensities for 2000–2020 were calculated and are shown in Table 3.

According to Table 3, it is evident that urban heat intensity exhibits a gradual increase over time. In 2000, the value was 5.45 ℃, and in 2005, it slightly increased to 5.47 ℃, with no significant gap observed. However, it showed a sharp rising trend from 2005 to 2011 and increased by about 0.6 ℃ from 2011 to 2020.

4.3 Factors affecting the spatial patterns of NDVI and NDBI on Zhoushan Island

In previous studies, it has been speculated that LST is strongly correlated with surface vegetation and urban built-up areas (areas with high vegetation coverage usually have lower land surface temperature, while areas with high density in urban built-up areas usually have higher LST). Therefore, the retrieved LST is correlated with *NDVI* and *NDBI*. The calculated correlation coefficients between them are shown in Table 4.

Table 4 shows that the absolute value of the correlation coefficient between *LST* and *NDVI* shows a downward trend. The negative correlation between *LST* and *NDVI* gradually weakened, but still remained negative. Despite the downward trend, their correlation coefficients maintained a relatively high absolute value, indicating a significant correlation between *LST* and *NDVI*. On the other hand, there is a positive correlation between *LST* and *NDBI*: with the increase in *NDBI*, *LST* shows a rising trend, while the decrease in urban construction leads to the decrease in *LST*.

Table 3
Urban heat intensities from 2000 to 2020 (℃).

Years	Average temperature in area covered with vegetation	Average temperature in area covered with urban built-up	Urban heat intensity
2000	30.49	35.94	5.45
2005	29.26	34.74	5.47
2011	29.21	37.96	8.74
2015	35.09	43.51	8.42
2020	38.09	47.45	9.36

Table 4
Correlation coefficients between LST and indices.

Years	NDVI correlation coefficient	NDBI correlation coefficient
2000	−0.6639	0.7043
2005	−0.6849	0.7765
2011	−0.8018	0.8322
2015	−0.7157	0.6698
2020	−0.6977	0.7577

5. Discussion

5.1 Reliability of the methodology

Using Landsat satellite images, we retrieve the LST of Zhoushan Island, produce the spatial and temporal distribution maps of LST, and divide the urban heat-island level. Landsat satellites have created the longest continuous Earth observation dataset with nearly 50 years of consistent high-quality scientific data in terms of spatial resolution, calibration capabilities, and spectral characteristics, providing accurate data for UHI studies.

The Pearson correlation is sensitive to linear relationships. It can accurately express the relationship between two variables and has good mathematical performance. It is widely used in statistics, social science, natural science, economics and other fields. It can help to accurately and deeply analyze the relationship between *LST* and various indices.

5.2 Uncertainty of the results

There are some uncertainties in the annual LST retrieved from Landsat satellite imagery. In this study, five high-quality images were selected to analyze the UHI effect of Zhoushan Island, such that the influence of cloud cover on LST retrieval was reduced as much as possible. However, excessive cloud cover adversely impacts the availability of high-quality images that can be selected.

6. Conclusions

In this study, Landsat satellite data were used to prepare the spatiotemporal distribution map of Zhoushan Island surface temperature, and the mean-standard deviation method was used to classify the UHI and monitor the spatiotemporal changes of UHI. Finally, the correlations between *LST* and the *NDVI*, as well as between *LST* and the *NDBI*, were analyzed. The conclusions are as follows.

(1) The average LST on Zhoushan Island shows an increasing trend. The high temperature areas are mainly distributed in the dense urban areas along the coast, while the low temperature areas are mainly distributed in high vegetation cover areas in the interior. The high temperature areas gradually concentrate in the coastal areas.
(2) According to the grade distribution and proportions of heat-island areas, weak heat-island areas and weaker heat-island areas are stable, and the moderate-temperature areas show a decreasing trend, indicating that they are gradually transforming into higher level heat-island areas. The proportion of heat-island areas shows an increasing trend, and the change is most significant in 2011. The no heat-island areas are mainly distributed in the inner areas with high vegetation cover, while the areas of high heat-island level are mainly distributed in the coastal highly urbanized areas. In general, the grades of UHIs on Zhoushan Island show a decreasing trend from the periphery to the inner part of the island.

(3) The urban heat intensity in Zhoushan Island escalated from 5.5 °C in 2000 to 9.4 °C in 2020, demonstrating a gradual intensification of the UHI effect. The UHI grade distribution map, LST retrieval map, and urban heat intensity have not changed significantly since 2011, indicating that the UHI effect in Zhoushan Island has stabilized since 2011.
(4) There are high correlations between *LST* and *NDVI*, as well as between *LST* and *NDBI*. *LST* is negatively correlated with vegetation coverage and positively correlated with construction coverage.

The distribution of the intensities of the urban heat-island areas is heterogeneous and is closely related to human activities and economic development. UHIs interact with the urban climate, but atmospheric factors do not exist in isolation, and the urban heat intensity does not affect the UHI effect independently. Therefore, the study of the relationship between UHI and urban pollution islands and their joint role in urban climate should also be an important direction for future urban heat-island research.

Acknowledgments

This work was supported by the National Natural Science Foundation of China (Grant No. 42171311). The authors declare that they have no known competing financial interests or personal relationships that could have appeared to affect the work reported in this paper.

References

1 R. Seager, M. Cane, N. Henderson, D. E. Lee, R. Abernathey, and H. Zhang: Nat. Clim. Change. **9** (2019) 517. https://doi.org/10.1038/s41558-019-0505-x
2 N. Mijani, S. K. Alavipanah, M. K. Firozjaei, J. J. Arsanjani, S. Hamzeh, and Q. Weng: Ecol. Indic. **117** (2020) 106555. https://doi.org/10.1016/j.ecolind.2020.106555
3 C. P. Morice, J. J. Kennedy, N. A. Rayner, J. Winn, E. Hogan, R. Killick, R. Dunn, T. Osborn, P. Jones, and I. Simpson: J. Geophys. Res.: Atmos. **126** (2021) e2019JD032361. https://doi.org/10.1029/2019JD032361
4 J. Luo, G. Ni, Y. Zhang, K. Wang, M. Shen, Z. Cao, T. Qi, Q. Xiao, Y. Qiu, Y. Cai, and H. Duan: Remote Sens. Environ. **287** (2023) 113480. https://doi.org/10.1016/j.rse.2023.113480
5 X. Chen, H. Zhao, P. Li, and Z. Yin: Remote Sens. Environ. **104** (2006) 133. https://doi.org/10.1016/j.rse.2005.11.016
6 C. Yang, F. Yan, and S. Zhang: J. Environ. Manage. **265** (2020) 110563. https://doi.org/10.1016/j.jenvman.2020.110563
7 R. Lyu, J. Pang, X. Tian, W. Zhao, and J. Zhang: Sustainable Cities Soc. **88** (2023) 104287. https://doi.org/10.1016/j.scs.2022.104287
8 X. Yang, P. Li, and Z. H. Wang: J. Environ. Manage. **344** (2023) 118452. https://doi.org/10.1016/j.jenvman.2023.118452
9 A. Guo, J. Yang, X. Xiao, J. Xia, C. Jin, and X. Li: Sustainable Cities Soc. **53** (2020) 101972. https://doi.org/10.1016/j.scs.2019.101972
10 J. Yang, Y. Wang, C. Xiu, X. Xiao, J. Xia, and C. Jin: J. Cleaner Prod. **275** (2020) 123767. https://doi.org/10.1016/j.jclepro.2020.123767
11 M. J. Nieuwenhuijsen: Environ. Int. **157** (2021) 106850. https://doi.org/10.1016/j.envint.2021.106850
12 F. Despini, C. Ferrari, G. Santunione, S. Tommasone, A. Muscio, and S. Teggi: Urban Clim. **35** (2021) 100761. https://doi.org/10.1016/j.uclim.2020.100761
13 G. Xian, H. Shi, Q. Zhou, R. Auch, K. Gallo, Z. Wu, and M. Kolian: Remote Sens. Environ. **269** (2022) 112803. https://doi.org/10.1016/j.rse.2021.112803
14 W. Peng, R. Wang, J. Duan, W. Gao, and Z. Fan: Urban Clim. **42** (2022) 101136. https://doi.org/10.1016/j.uclim.2022.101136

15 Y. Wang, D. O. Hessen, B. H. Samset, and F. Stordal: Remote Sens. Environ. **280** (2022) 113181. https://doi.org/10.1016/j.rse.2022.113181
16 H. Du, W. Zhan, Z. Liu, J. Li, L. Li, J. Lai, S. Miao, F. Huang, C. G. Wang, and C. L. Wang: ISPRS J. Photogramm. Remote Sens. **181** (2021) 67. https://doi.org/10.1016/j.isprsjprs.2021.09.003
17 S. W. Kim, and R. D. Brown: Renewable Sustainable Energy Rev. **148** (2021) 111256. https://doi.org/10.1016/j.rser.2021.111256
18 R. Yao, L. Wang, X. Huang, Y. Liu, Z. Niu, S. Wang, and L. Wang: Sci. Total Environ. **772** (2021) 145607. https://doi.org/10.1016/j.scitotenv.2021.145607
19 C. Chen, J. Liang, G. Yang, and W. Sun: Ocean Coastal Manage. **238** (2023) 106554. https://doi.org/10.1016/j.ocecoaman.2023.106554
20 H. Fu, G. Sun, L. Zhang, A. Zhang, J. Ren, X. Jia, and F. Li: ISPRS J. Photogramm. Remote Sens. **203** (2023) 115. https://doi.org/10.1016/j.isprsjprs.2023.07.013
21 A. Tariq, F. Mumtaz, X. Zeng, M. Y. J. Baloch, and M. F. U. Moazzam: Remote Sens. Appl.: Soc. Environ. **27** (2022) 100779. https://doi.org/10.1016/j.rsase.2022.100779
22 C. Yan, Q. Guo, H. Li, L. Li, and G. Y. Qiu: Build. Environ. **169** (2020) 106541. https://doi.org/10.1016/j.buildenv.2019.106541
23 G. Chen, Y. Chen, X. Tan, L. Zhao, Y. Cai, and L. Li: Build. Environ. **244** (2023) 110770. https://doi.org/10.1016/j.buildenv.2023.110770
24 F. B. Errebai, D. Strebel, J. Carmeliet, and D. Derome: Energy Build. **273** (2022) 112410. https://doi.org/10.1016/j.enbuild.2022.112410
25 B. Halder, J. Bandyopadhyay, and P. Banik: Sustainable Cities Soc. **74** (2021) 103186. https://doi.org/10.1016/j.scs.2021.103186
26 J. Lai, W. Zhan, J. Voogt, J. Quan, F. Huang, J. Zhou, B. Bechtel, L. Hu, K. Wang, and C. Cao: Remote Sens. Environ. **253** (2021) 112198. https://doi.org/10.1016/j.rse.2020.112198
27 W. Wang, K. Liu, R. Tang, and S. Wang: Phys. Chem. Earth, Parts A/B/C **110** (2019) 168. https://doi.org/10.1016/j.pce.2019.01.002
28 Z. Li, H. Wu, S. Duan, W. Zhao, H. Ren, X. Liu, P. Leng, R. Tang, X. Ye, and J. Zhu: Rev. Geophys. **61** (2023) e2022RG000777. https://doi.org/10.1029/2022RG000777
29 Z. Wang: Sustainable Cities Soc. **77** (2022) 103581. https://doi.org/10.1016/j.scs.2021.103581
30 J. Yang, J. Ren, D. Sun, X. Xiao, J. C. Xia, C. Jin, and X. Li: Sustainable Cities Soc. **69** (2021) 102818. https://doi.org/10.1016/j.scs.2021.102818
31 S. B. Jallu, R. U. Shaik, R. Srivastav, and G. Pignatta: Energy Nexus. **5** (2022) 100056. https://doi.org/10.1016/j.nexus.2022.100056
32 A. A. Jamali, R. G. Kalkhajeh, T. O. Randhir, and S. He: J. Environ. Manage. **302** (2022) 113970. https://doi.org/10.1016/j.jenvman.2021.113970
33 J. Luo, Z. Sun, L. Lu, Z. Xiong, L. Cui, and Z. Mao: J. Environ. Manage. **315** (2022) 115100. https://doi.org/10.1016/j.jenvman.2022.115100
34 G. Sun, Z. Pan, A. Zhang, X. Jia, J. Ren, H. Fu, and K. Yan: IEEE Trans. Geosci. Remote Sens. **61** (2023) 5519915. https://doi.org/10.1109/TGRS.2023.3292065
35 M. Jia, H. Zeng, Z. Chen, Z. Wang, C. Ren, D. Mao, C. Zhao, R. Zhang, and Y. Wang: Remote Sens. Environ. **305** (2024) 114104. https://doi.org/10.1016/j.rse.2024.114104
36 E. Neinavaz, M. Schlerf, R. Darvishzadeh, M. Gerhards, and A. K. Skidmore: Int. J. Appl. Earth Obs. Geoinf. **102** (2021) 102415. https://doi.org/10.1016/j.jag.2021.102415
37 C. Chen, J. Liang, F. Xie, Z. Hu, W. Sun, G. Yang, J. Yu, L. Chen, L. H. Wang, L. Y. Wang, H. Chen, X. He, and Z. Zhang: Int. J. Appl. Earth Obs. Geoinf. **107** (2022) 102711. https://doi.org/10.1016/j.jag.2022.102711
38 J. Luo, G. Ni, Y. Zhang, K. Wang, M. Shen, Z. Cao, T. Qi, Q. Xiao, Y. Qiu, Y. Cai, and H. Duan: Remote Sens. Environ. **287** (2023) 113480. https://doi.org/10.1016/j.rse.2023.113480
39 M. Yasir, S. Liu, X. Ming, J. Wan, S. Pirasteh, and K. B. Dang: IEEE Trans. Geosci. Remote Sens. **62** (2024) 5202613. https://doi.org/10.1109/tgrs.2024.3352150
40 C. R. D. Almeida, A. C. Teodoro, and A. Gonçalves: Environments **8** (2021) 105. https://doi.org/10.3390/environments8100105
41 M. Jia, Z. Wang, D. Mao, C. Ren, K. Song, C. Zhao, C. Wang, X. Xiao, and Y. Wang: Sci. Bull. **68** (2023) 1306. https://doi.org/10.1016/j.scib.2023.05.004
42 J. Liang, C. Chen, Y. Song, W. Sun, and G. Yang: Sustainable Horiz. **7** (2023) 100061. https://doi.org/10.1016/j.horiz.2023.100061
43 F. Wang, Z. Qin, C. Song, L. Tu, A. Karnieli, and S. Zhao: Remote Sens. **7** (2015) 4268. https://doi.org/10.3390/rs70404268

44 Z. Wei, X. Jiao, Y. Du, J. Zhang, H. Pan, G. Wang, D. Wang, and Y. P. Wang: Ocean Coastal Manage. **237** (2023) 106516. https://doi.org/10.1016/j.ocecoaman.2023.106516

45 W. Cao, R. Li, X. Chi, N. Chen, J. Chen, H. Zhang, and F. Zhang: Ecol. Indic. **76** (2017) 1. https://doi.org/10.1016/j.ecolind.2017.01.001

46 C. Chen, J. Fu, S. Zhang, and X. Zhao: Estuarine Coastal Shelf Sci. **217** (2019) 281. https://doi.org/10.1016/j.ecss.2018.10.021

47 M. G. Tulbure, M. Broich, V. Perin, M. Gaines, J. Ju, S. V. Stehman, T. Pavelsky, J. G. Masek, S. Yin, and J. Mai: ISPRS J. Photogramm. Remote Sens. **185** (2022) 232. https://doi.org/10.1016/j.isprsjprs.2022.01.021

48 M. A. Wulder, D. P. Roy, V. C. Radeloff, T. R. Loveland, M. C. Anderson, D. M. Johnson, S. Healey, Z. Zhu, T. A. Scambos, N. Pahlevan, M. Hansen, N. Gorelick, C. J. Crawford, J. G. Masek, T. Hermosilla, J. C. White, A. S. Belward, C. Schaaf, C. E. Woodcock, J. L. Huntington, L. Lymburner, P. Hostert, F. Gao, A. Lyapustin, J. F. Pekel, P. Strobl, and B. D. Cook: Remote Sens. Environ. **280** (2022) 113195. https://doi.org/10.1016/j.rse.2022.113195

49 K. Kinch, M. Madsen, J. Bell, J. N. Maki, Z. Bailey, A. Hayes, O. Jensen, M. Merusi, M. Bernt, A. Sørensen, M. Hilverda, E. Cloutis, D. Applin, E. Mateo-Marti, J. A. Manrique, G. Lopez-Reyes, A. Bello-Arufe, B. L. Ehlmann, J. Buz, A. Pommerol, N. Thomas, L. Affolter, K. E. Herkenhoff, J. R. Johnson, M. Rice, P. Corlies, C. Tate, M. A. Caplinger, E. Jensen, T. Kubacki, E. Cisneros, K. Paris, and A. Winhold: Space Sci. Rev. **216** (2020) 1. https://doi.org/10.1007/s11214-020-00774-8

50 M. Yang, Y. Hu, H. Tian, F. A. Khan, Q. Liu, J. I. Goes, H. D. R. Gomes, and W. Kim: Remote Sens. **13** (2021) 5062. https://doi.org/10.3390/rs13245062

51 E. Parlow: Remote Sens. **13** (2021) 3598. https://doi.org/10.3390/rs13183598

52 B. Yuan, L. Zhou, X. Dang, D. Sun, F. Hu, and H. Mu: J. Environ. Manage. **295** (2021) 113116. https://doi.org/10.1016/j.jenvman.2021.113116

53 L. Mohammad, J. Bandyopadhyay, R. Sk, I. Mondal, T. T. Nguyen, G. F. C. Lama, and D. T. Anh: J. Environ. Manage. **343** (2023) 118226. https://doi.org/10.1016/j.jenvman.2023.118226

54 S. W. Kim, and R. D. Brown: Sci. Total Environ. **779** (2021) 146389. https://doi.org/10.1016/j.scitotenv.2021.146389